Supplement of The Cryosphere, 19, 5719–5761, 2025 https://doi.org/10.5194/tc-19-5719-2025-supplement © Author(s) 2025. CC BY 4.0 License.





## Supplement of

## The Greenland-Ice-Sheet evolution over the last 24 000 years: insights from model simulations evaluated against ice-extent markers

Tancrède P. M. Leger et al.

Correspondence to: Tancrède P. M. Leger (tancrede.leger@unil.ch)

The copyright of individual parts of the supplement might differ from the article licence.

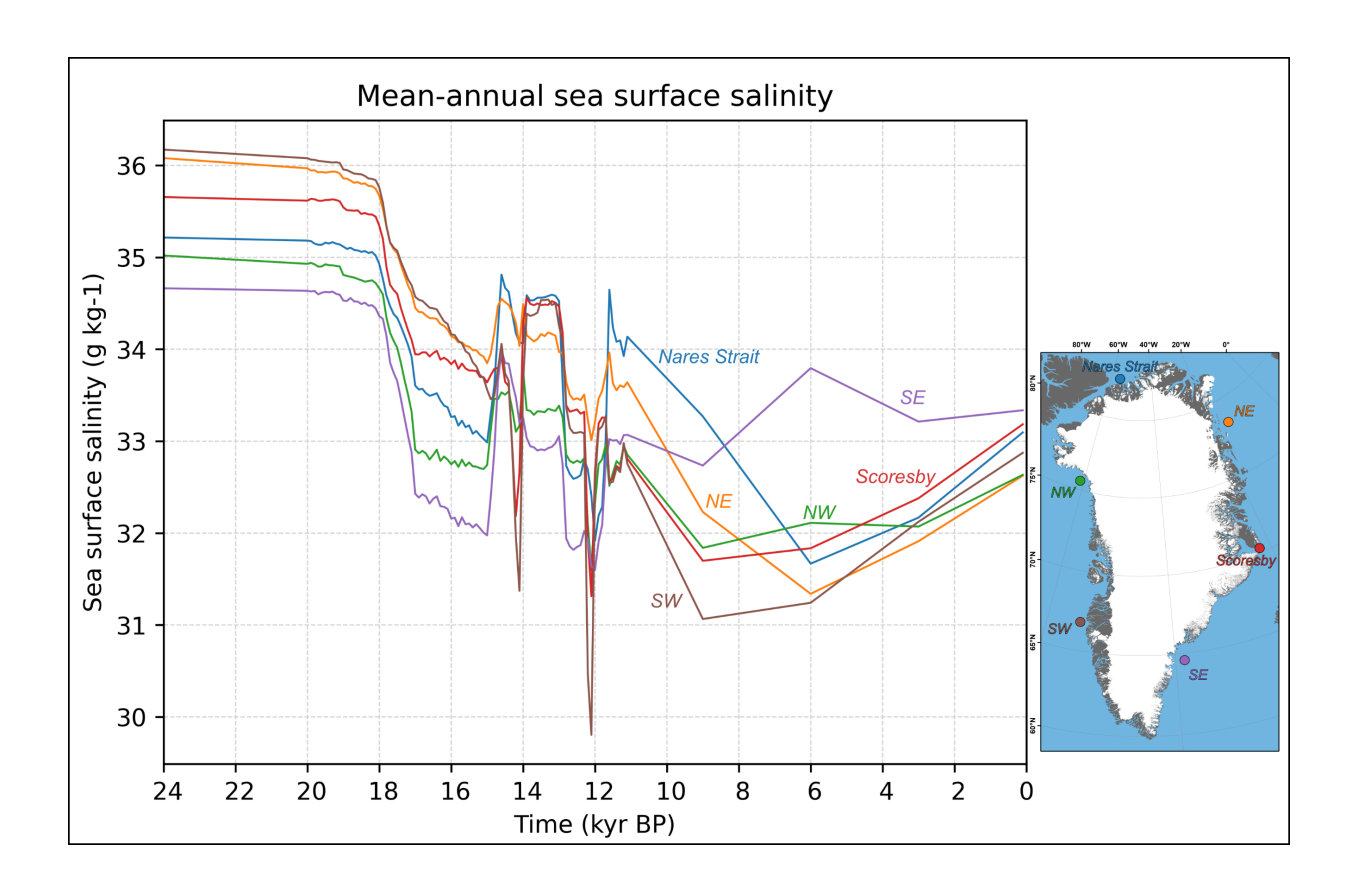


**Figure S1**. Time series of mean annual sea-surface salinity extracted from our two-dimensional input forcing fields, for six distinct locations taken from different ocean basins offshore the present-day GrIS (as shown by the inset map). The data are derived from iCESM transient and equilibrium time slice simulations (see methods section), with linear interpolation used to bridge temporal gaps between periods covered by these simulations.

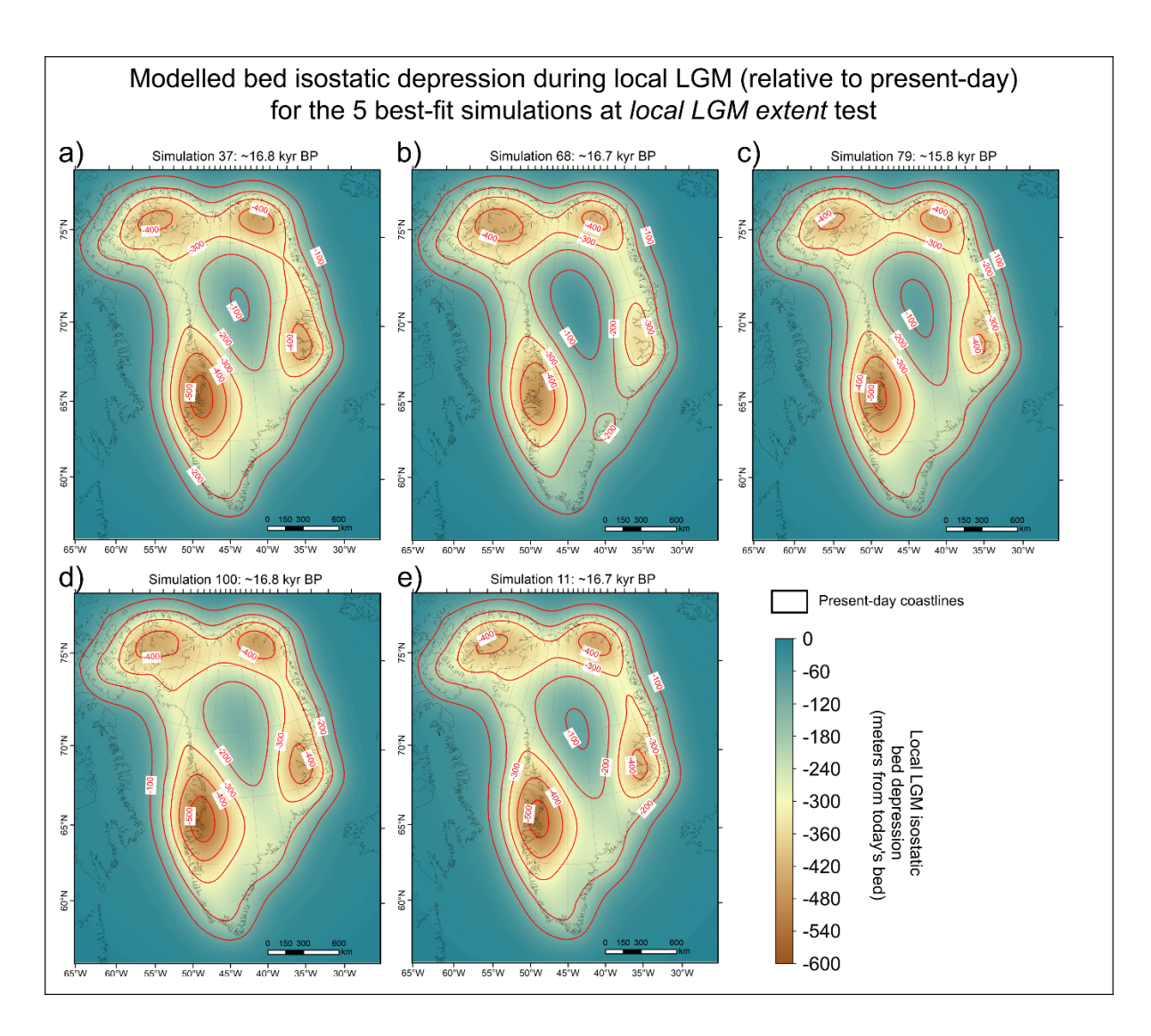


**Figure S2**. Modelled bed isostatic depression during the local LGM (timing is simulation-dependent), relative to the present-day bed topography, for the 5 best-scoring ensemble simulations at the *local LGM extent* test.

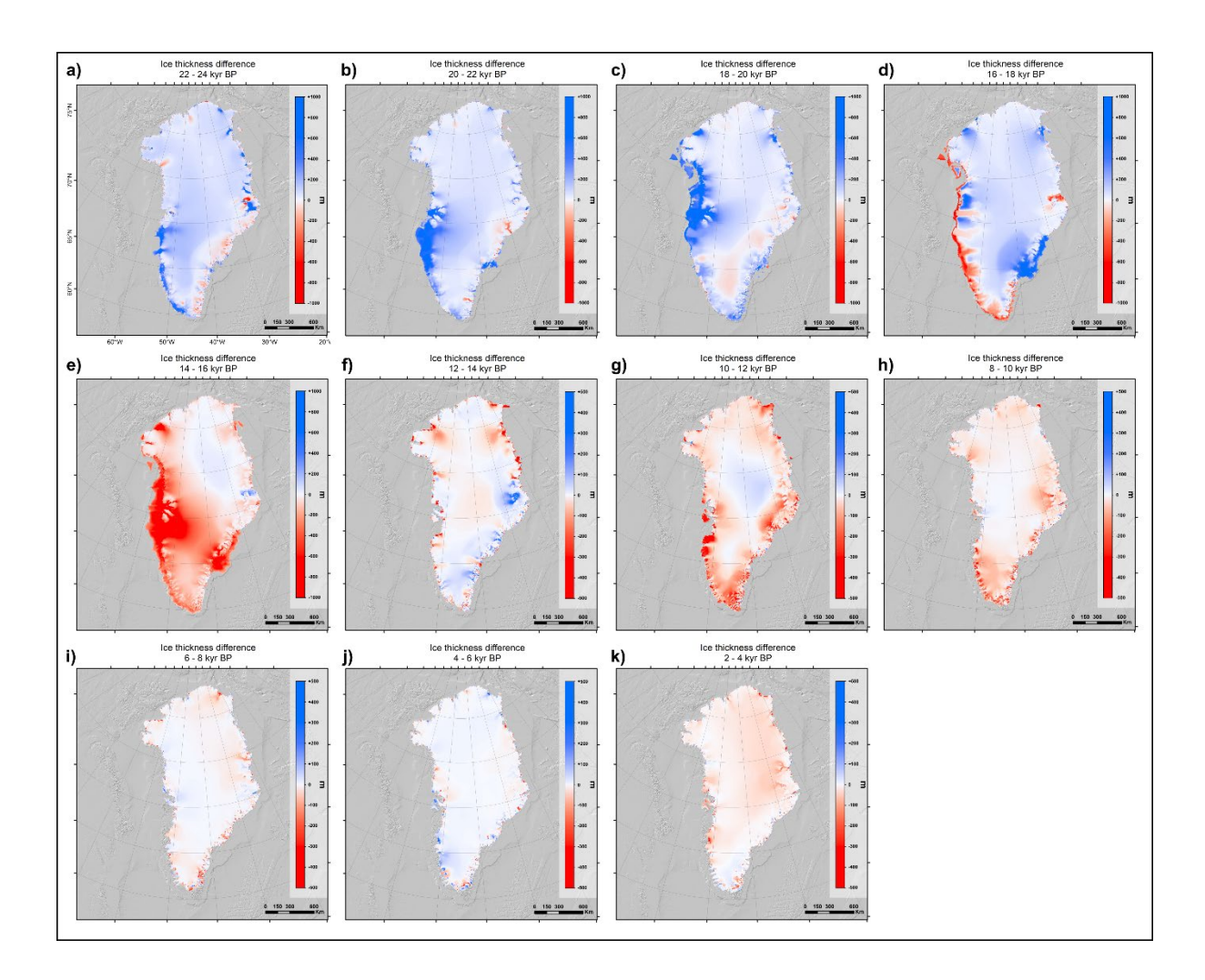


**Figure S3**. 2 kyr ice thickness difference maps between 24 - 22 and 4 - 2 kyr BP for one of the 5 overall best-fit simulations (which passes all sieves); simulation number 26. Note that the ice-thickness-difference colorbar minimum and maximum values are different between panels a - e (range: +1000; - 1000), and panels f - k (range: +500; -500).

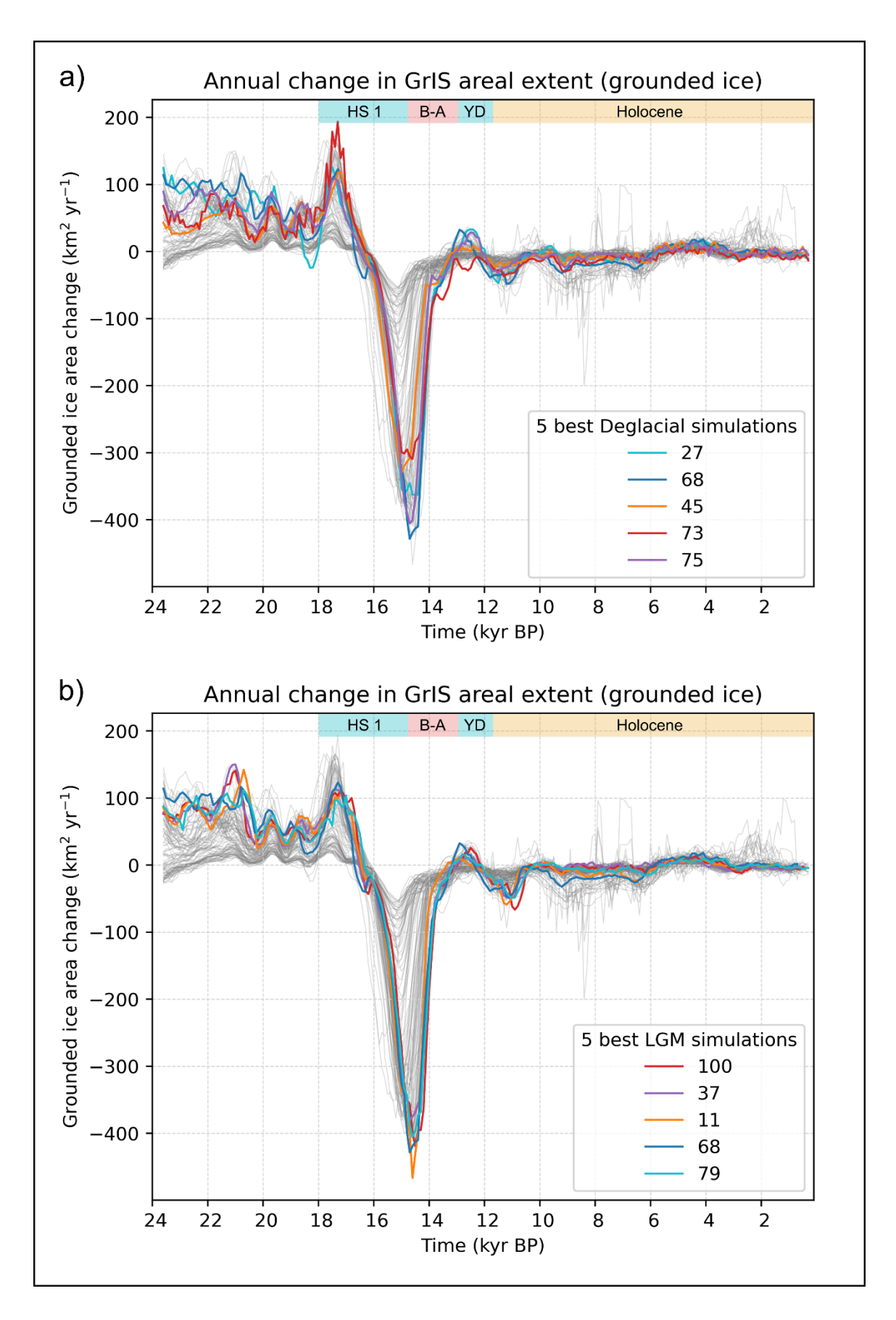


**Figure S4**. Ensemble time series (thin grey lines) of modelled annual change in GrIS-wide grounded ice areal extent, with best-scoring simulations at both the *deglacial extent* test (panel a) and the *local-LGM extent* test (panel b) highlighted with thick coloured time series.

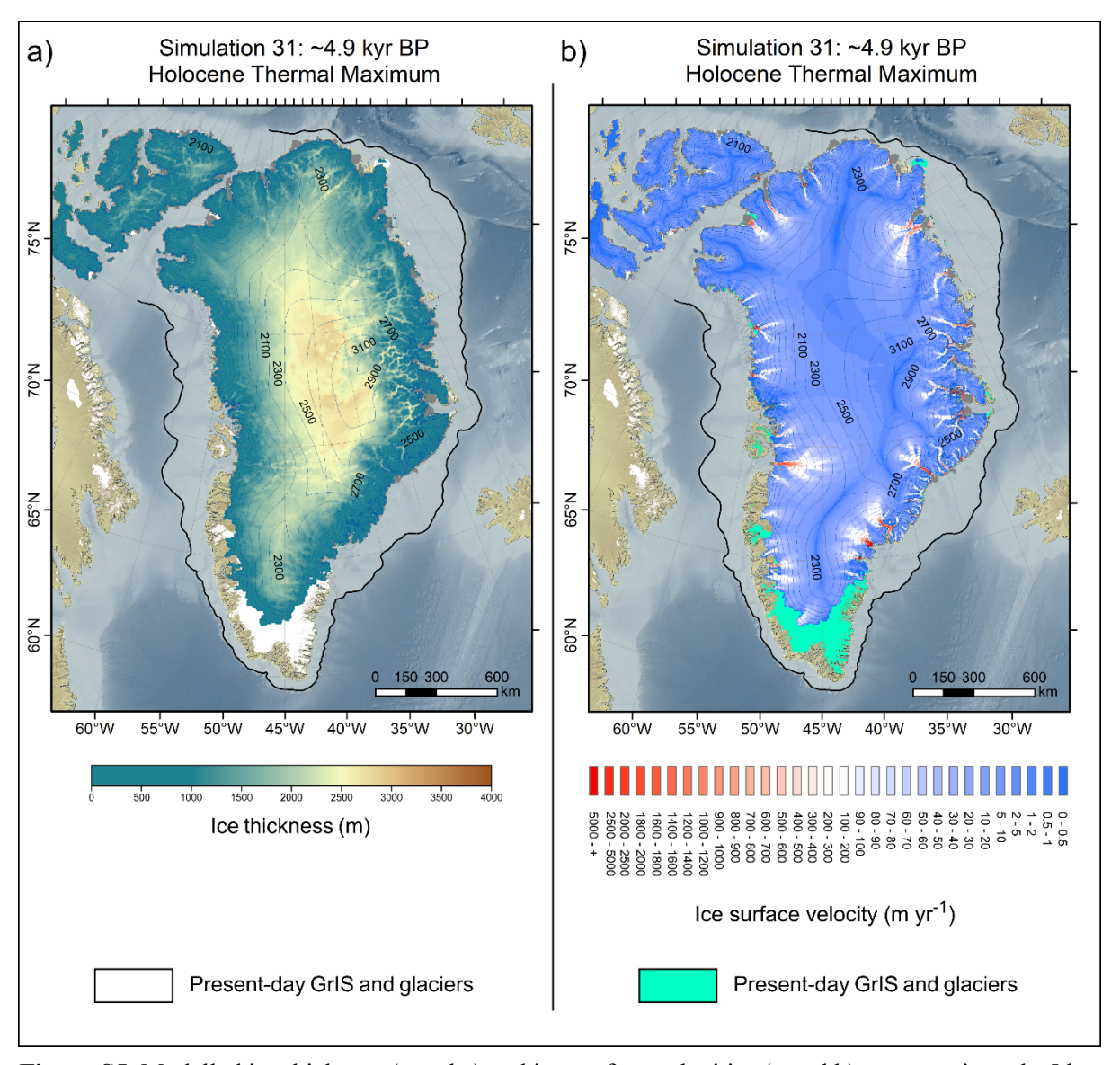


**Figure S5**. Modelled ice thickness (panel a) and ice-surface velocities (panel b) at approximately 5 kyr BP, during minimum Holocene ice extent, for the best-scoring ensemble simulation at the PI-extent test, *i.e.* simulation 31. This figure highlights the magnitude of retreat of modelled GrIS margins following the Holocene Thermal Maximum, in some regions reaching behind the present-day GrIS margin (in white (panel a) or bright green (panel b)). On both panels, contour lines are 200 m ice-surface elevation contour intervals.

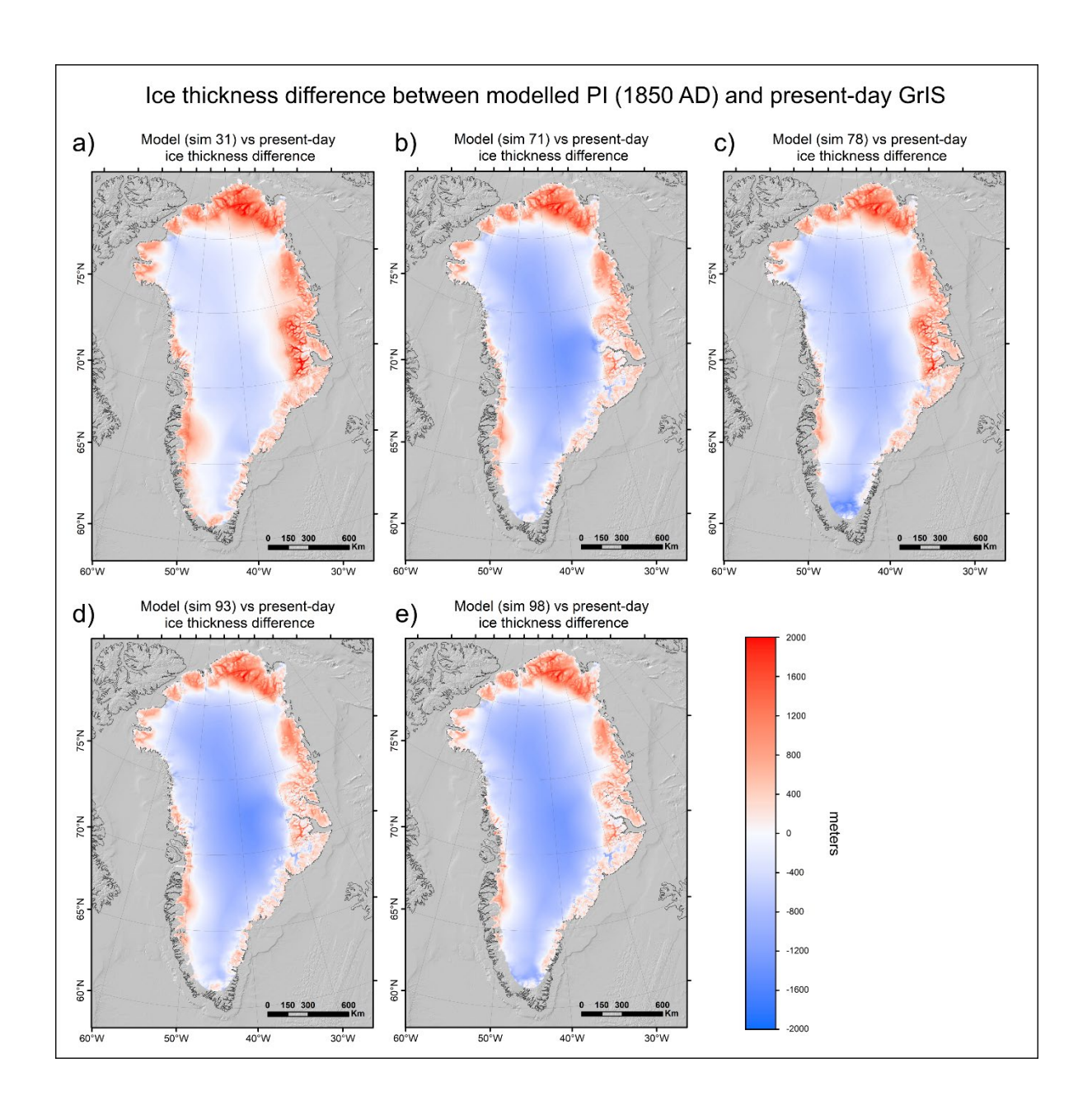


**Figure S6**. GrIS thickness difference between modelled PI states (1850 AD) versus the reconstructed present-day GrIS ice thickness (BedMachine v4: Morlighem et al., 2017) for the 5 best-scoring simulations at the *PI extent* test.

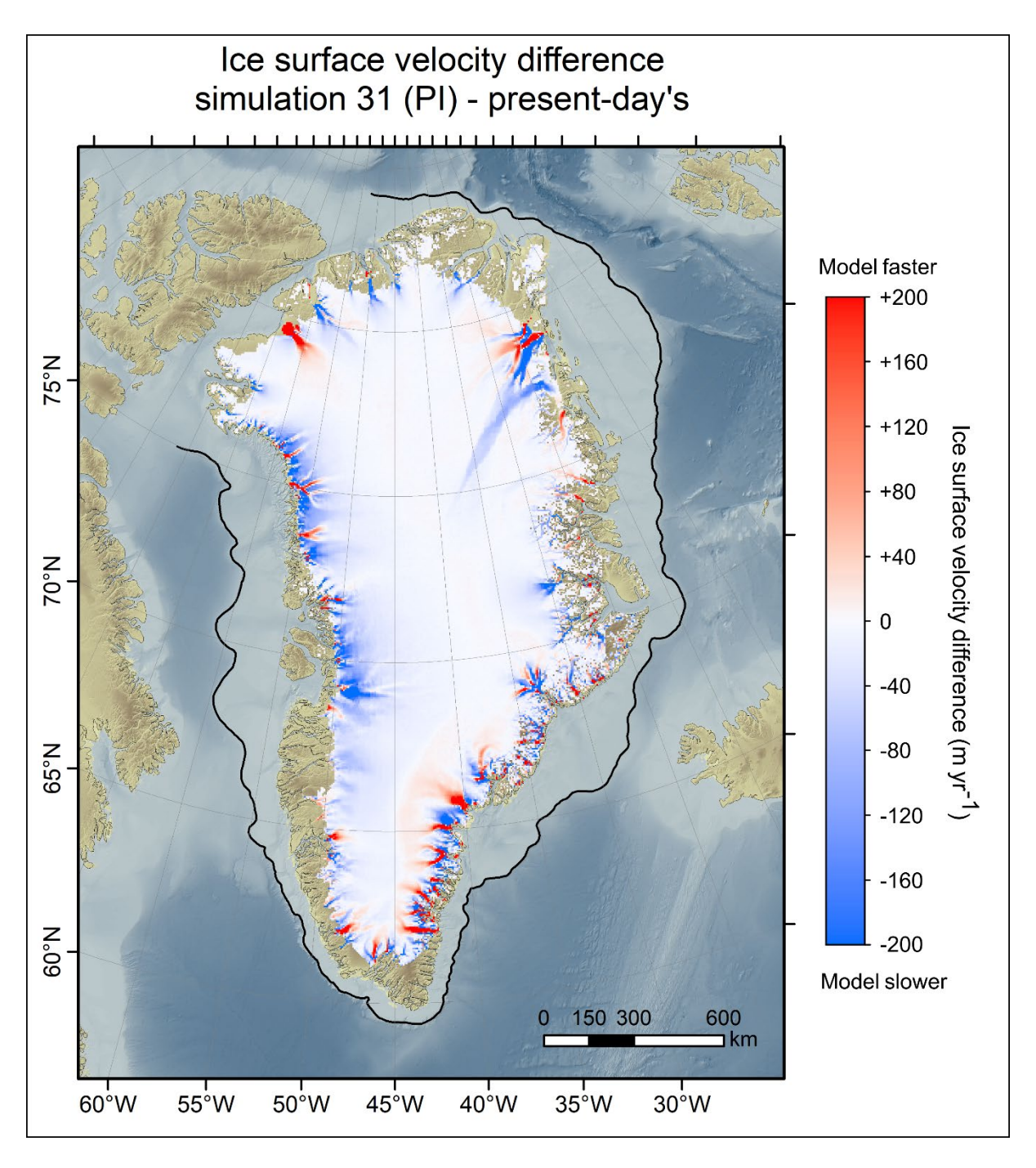


**Figure S7**. Modelled ice-surface velocity difference between modelled PI state (1850 AD) for the best-scoring simulation at the PI extent test (i.e. simulation 31) versus observed present-day ice surface velocities of the GrIS (Joughin et al., 2018).

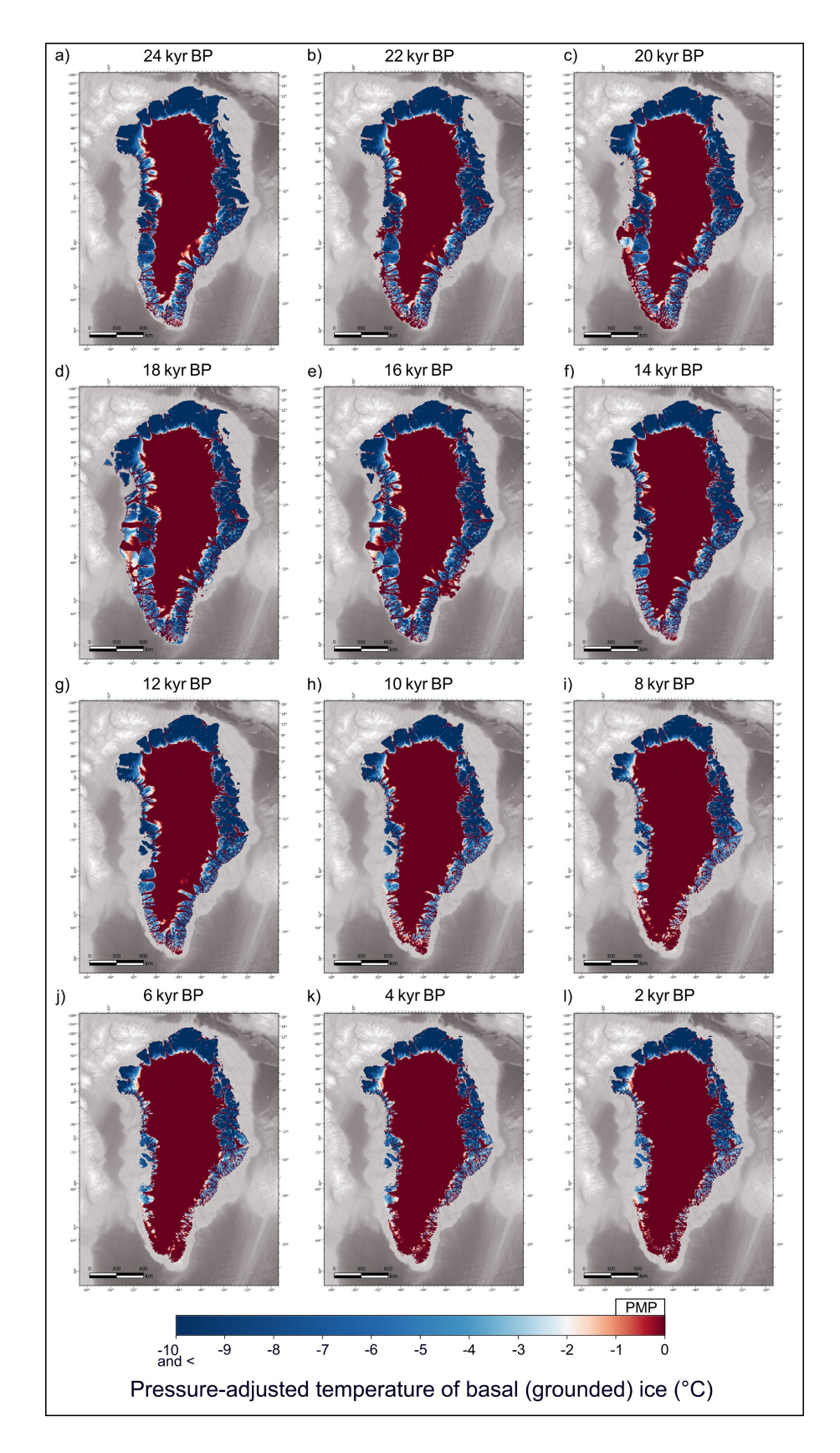


**Figure S8**. Pressure-adjusted modelled basal ice temperature of grounded ice for one of our ensemble's overall best-fit simulations (which passes all sieves: simulation number 26). The model output data is shown for timeslices every 2 kyr, between 24 and 2 kyr BP. 'PMP' stands for 'pressure-melting point'.

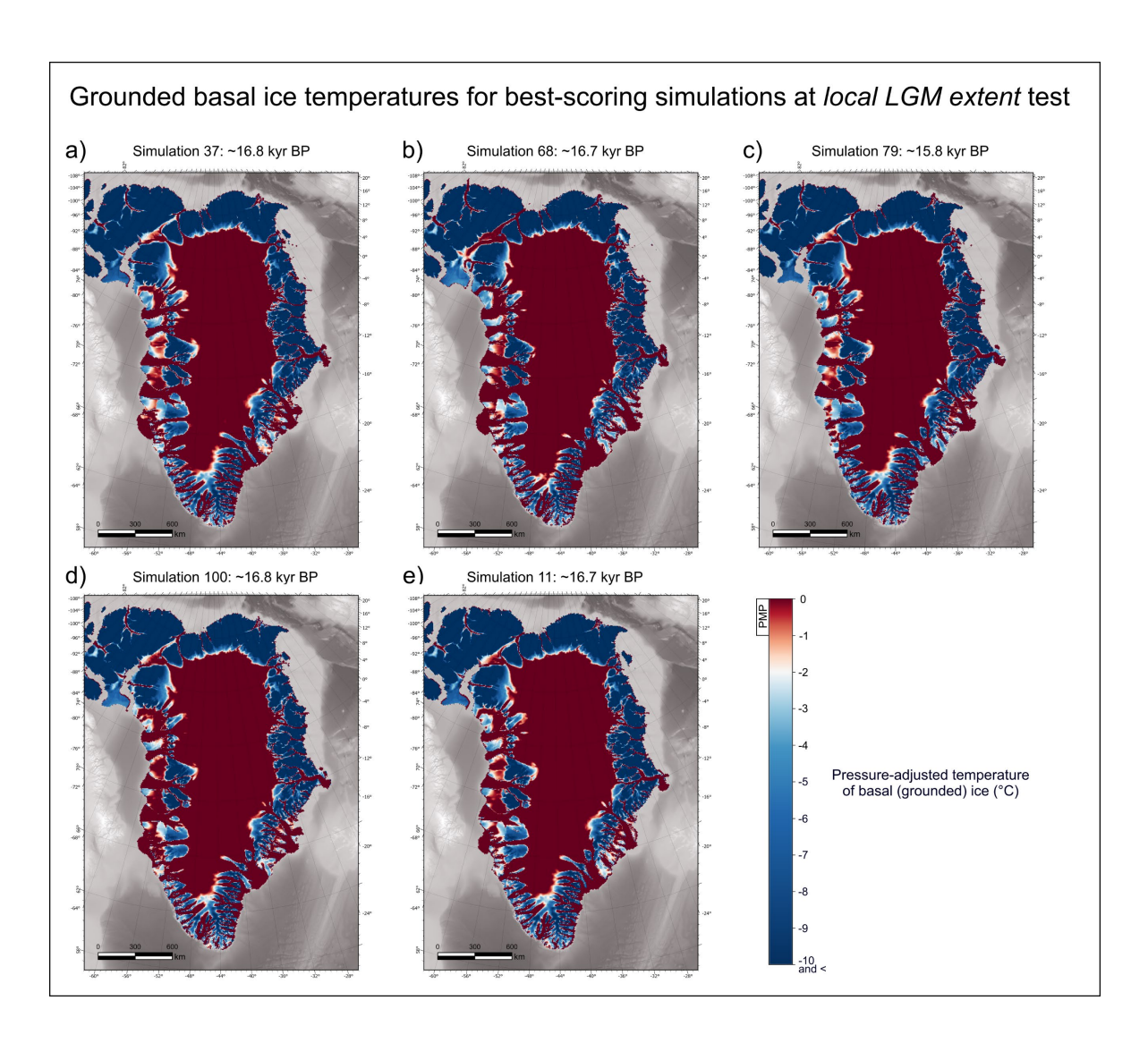


**Figure S9**. Modelled basal ice temperatures for grounded ice during the local LGM (timing is simulation-dependent) for the 5 best-scoring ensemble simulations at the *local LGM extent* test. 'PMP' stands for 'pressure-melting point'.

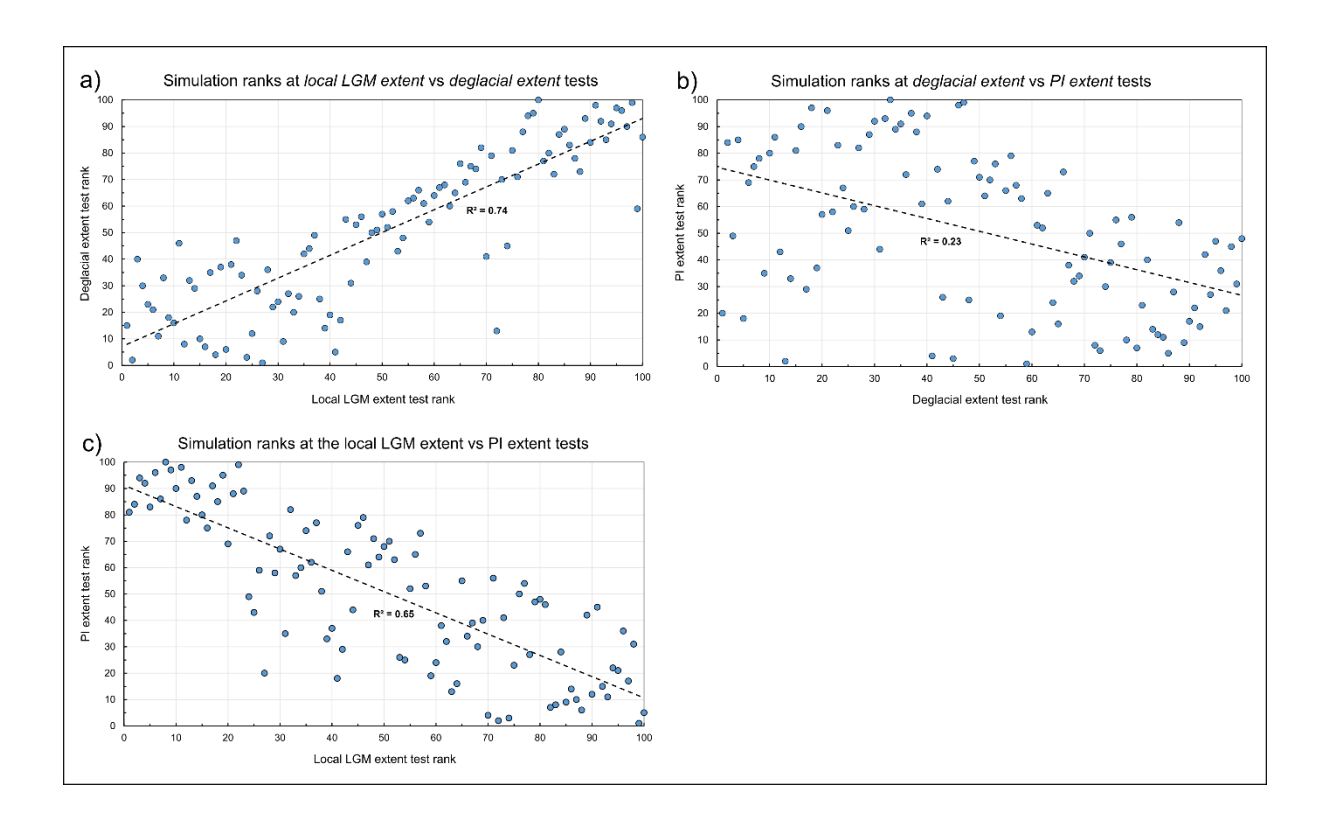


**Figure S10**. Linear regressions between ensemble simulation relative ranks at one of our three model-data comparison tests (*e.g. PI extent* test) versus another. A high rank (e.g. 1) is equivalent to the best-scoring simulation, while a low rank (e.g. 100) represents the worse-scoring simulation. Ensemble simulations that score well at the *local LGM extent* test also tend to score well at the *deglacial extent* test ( $R^2 = 0.74$ ) (panel a), for instance, while a negative correlation ( $R^2 = 0.65$ ) can be observed between *local LGM extent* test ranks and PI extent test ranks (panel c).

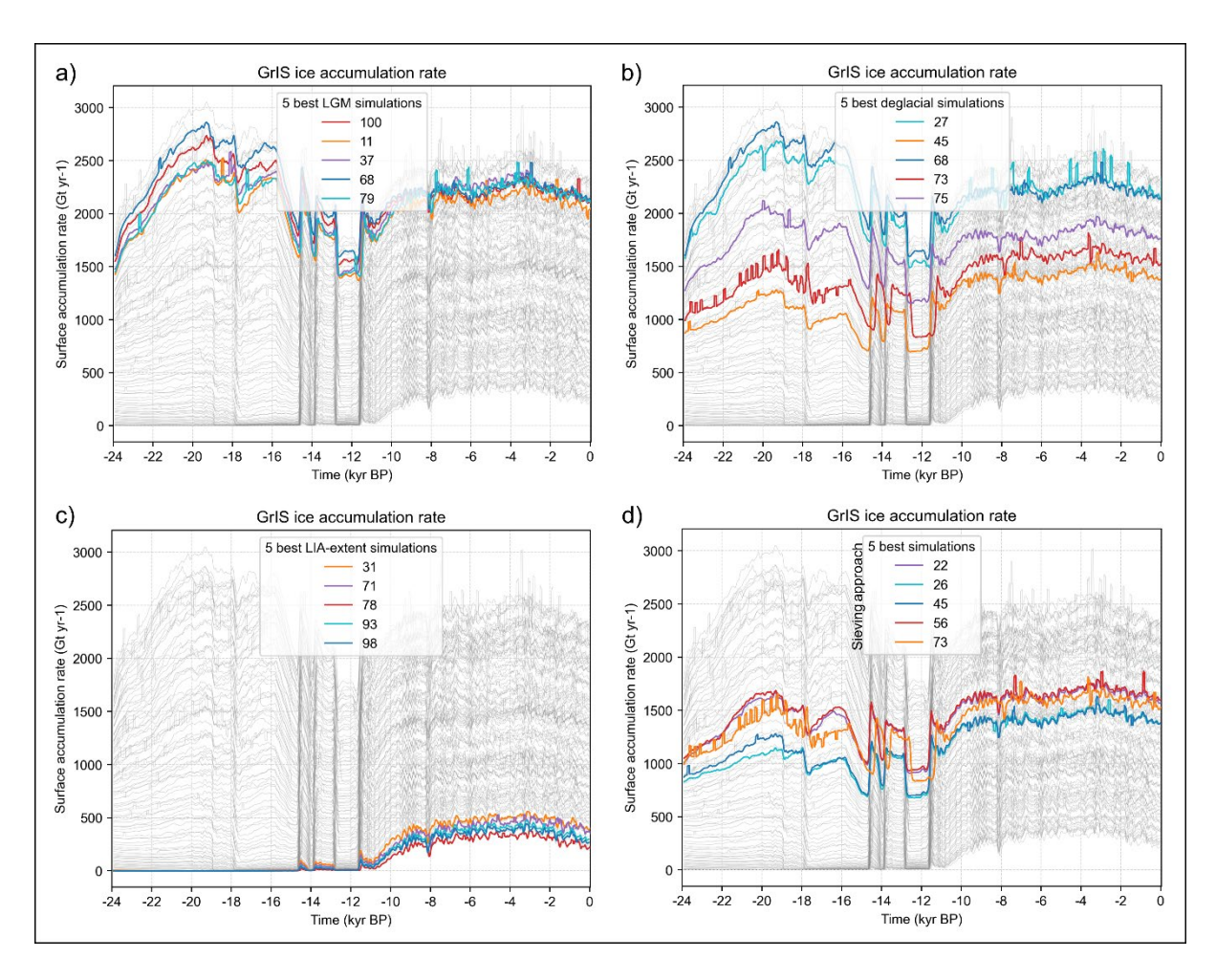


**Figure S11**: Ensemble time series of modelled GrIS-wide integrated ice accumulation rate. The best-scoring simulations at each of our three model-data comparison tests (panels a - c), and for the five overall best-fit simulations (which pass all sieves; panel d) highlighted in thick coloured time series.

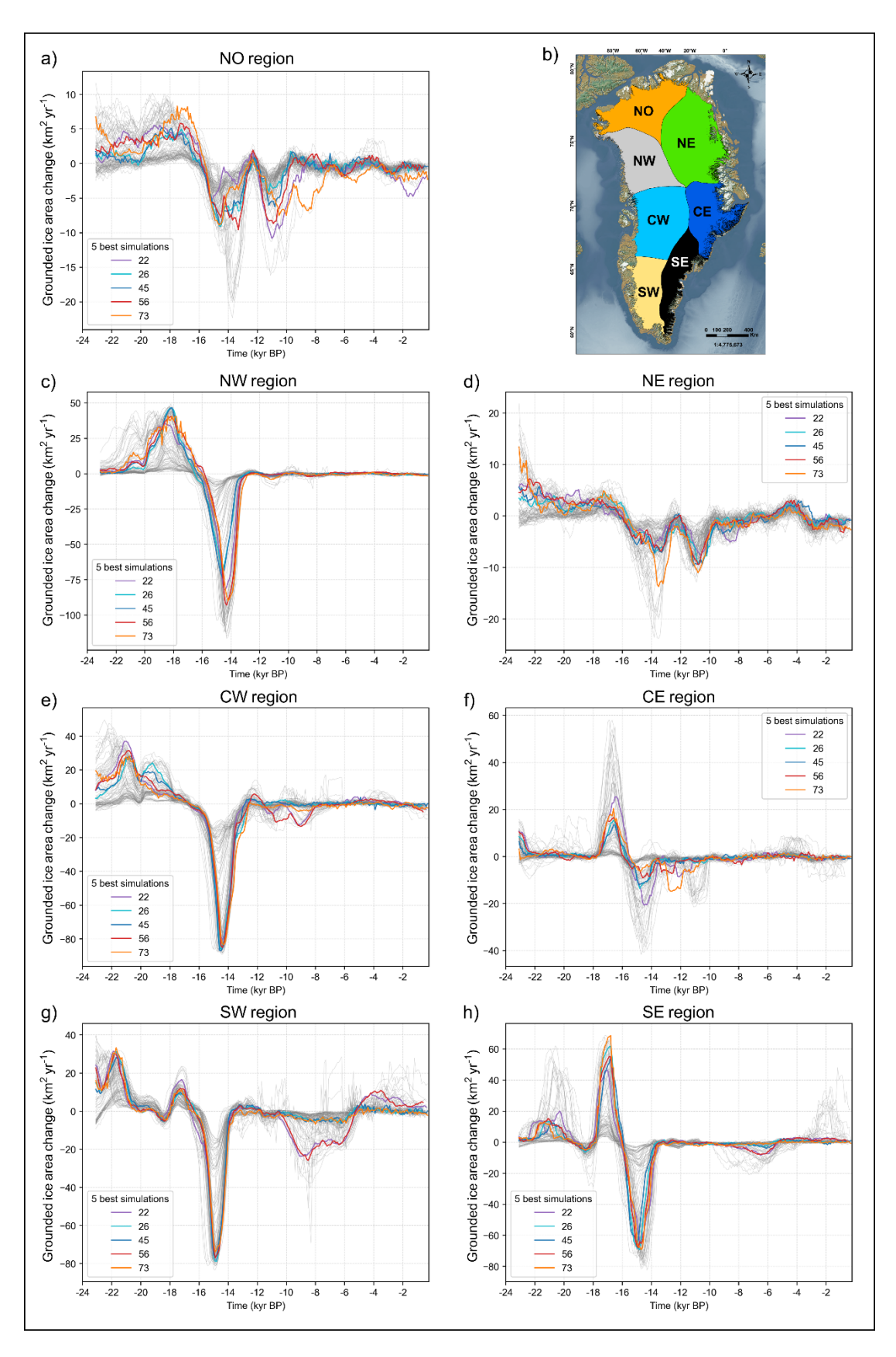


**Figure S12**: Ensemble time series (thin grey lines) of modelled annual change in GrIS-wide grounded ice area for each of the seven main GrIS regions (whose location are shown in panel b). The 5 overall best-fit simulations (which pass all sieves) are highlighted with thick coloured times series.

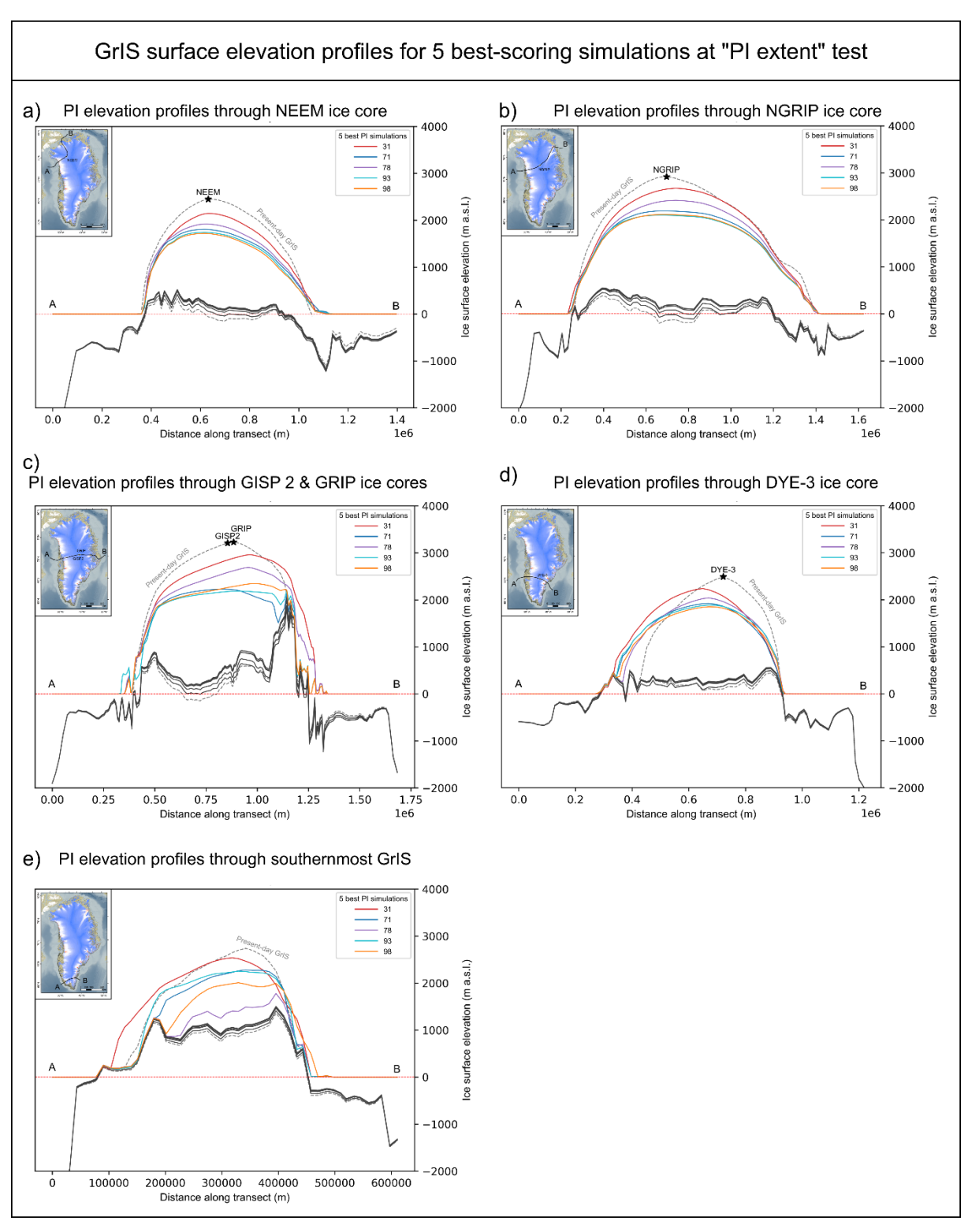


**Figure S13**: Modelled ice surface and bed elevations during the PI (1850 AD) extracted across five different transects for our five best-scoring simulations at the *PI extent* test (thicker coloured lines), and for the present-day GrIS (dashed grey lines). The four transects were drawn following modelled ice flow lines while ensuring to cross the NEEM (panel a), NGRIP (panel b), GISP 2 and GRIP (panel c), and the DYE-3 (panel d) ice core locations, as shown by the black lines in the inset maps. The transect drawn through the southernmost GrIS (panel e) was not drawn to cross any specific ice core locations, however.

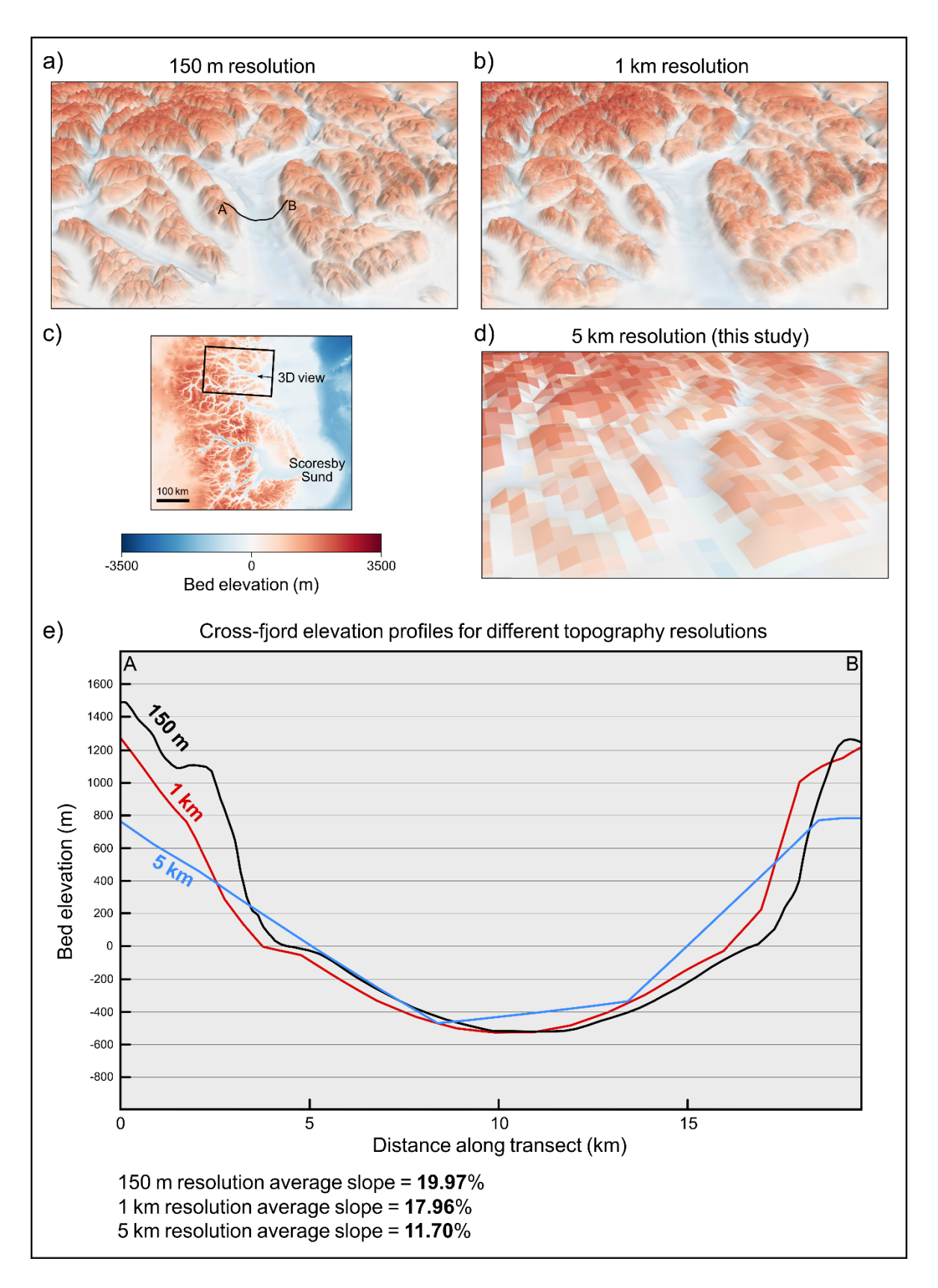


**Figure S14**: Three-dimensional views (panels a, b, and d) of bed topography (BedMachine v4 merged with GEBCO data) and cross elevation profiles (panel e) along a transect drawn across the Kangerluk Kejser Franz Joseph fjord (73.2°N; 23.2°W; black line in panel a). Elevation profiles are shown for three different grid resolutions (5 km, 1 km, and 150 m). While average slopes over such a terrain

decreases by 10% between 150 m and 1 km resolution grids, it decreases by around 40% between 150 m and 5 km resolution grid, 5 km being the model resolution of this study. For more details regarding the bed topography used in this modelling study, the reader is referred to Figure 1 and its caption.

## Further discussion on the topographic analysis:

We note that the CE and NE GrIS regions, where the greatest model-data misfits with PaleoGrIS 1.0 are found (Figs. 18, 22, 23), also present the highest concentration of high and steep topographies (1500 - 3000 m a.s.l.) in Greenland (Morlighem et al., 2017). We hypothesise that coarse model resolution may be a factor contributing to the higher relative iceextent misfits observed in these regions during the Late-Glacial and Holocene deglaciation. Indeed, a large portion of the Eastern Greenland coast features the steepest and highest mountain ranges of the continent, stretching from 67 °N (Schweizerland Alps) to 77 °N (Halle range), and dissected by a complex network of overdeepened valleys. This topographic setting leads to the highest concentration of deglaciated and relatively long (>100 km), narrow (<15 km), deep and steep-sided fjords in Greenland (Swift et al., 2008). These major fjord systems include the Kangertittivaq (Scoresby Sund), Kangerluk Kong Oscar, Kangerluk Kejser Franz Joseph (Figure S14), Gael Hamke Bay, Shannon Bay and Dove Bay (76°N) complexes. According to geochronological reconstructions, the retreat of GrIS outlet glaciers from the outer mouths of these CE and NE Greenland fjords to near their present-day positions occurred mainly between ~12 and ~8.5 kyr BP (e.g. Marienfeld, 1990; Bennike et al., 1999; Håkansson et al., 2007; Leger et al., 2024). However, the majority of this retreat is missing in our ensemble simulations.

A 5 x 5 km horizontal resolution may not be fine enough to capture the complexity of GrIS margin retreat into the complex network of over-deepened fjords and steep valleys of these regions. By drawing topographic elevation profiles across one the region's main fjords (Kangerluk Kejser Franz Joseph, 73.2°N; 23.2°W), we find that even for one of the widest NE Greenland fjords (~20 km), formerly acting as the main topographic conduit for the Waltershausen Glacier, the topography is heavily flattened at 5 km resolution (Figure S14). Across the profile, summit elevations of fjord-side mountains are underestimated by 30 - 50%, and average slope along the transect is 40% and 35% lower than for 150 m and 1 km resolution grids, respectively (Figure S14). Thus, at 5 x 5 km resolution, the modelled GrIS is less topographically constrained than it should be during deglacial margin retreat and thinning (Figure S14). A better resolved topography (e.g. 1 x 1 km or lower) would likely lead to both higher ice flux rates within narrow valleys, due to higher summits, steeper bed slopes, and greater ice flow convergence, but also to deeper fjords enabling more water ingress as modelled tidewater glaciers retreat. Both mechanisms, unlikely to be captured at 5 x 5 km, would together enhance modelled GrIS thinning and retreat rates during the Late-Glacial and early-to-mid Holocene in these regions. In such steep terrain, higher-resolution modelling may lead to better model-data fit for a given parameter configuration (Leger et al., 2025). This was in part shown by Aschwanden et al. (2016) who, using PISM, found that observed flow velocities of main present-day GrIS outlet glaciers (e.g. Nuussuup Sermia, Sermeq Kujalleq) were better matched using resolutions of 600 and 1500 m, relative to 3600 and 4500 m, with the latter causing maximum flow velocities to be underestimated by factors of 4 - 7. Therefore, while the inability to resolve fine topographies generates biases across the domain, we argue its negative impact on model-data fit is likely to be greater in CE and NE Greenland, relative to other regions, due to the greater concentration of steep and high-relief topographies.

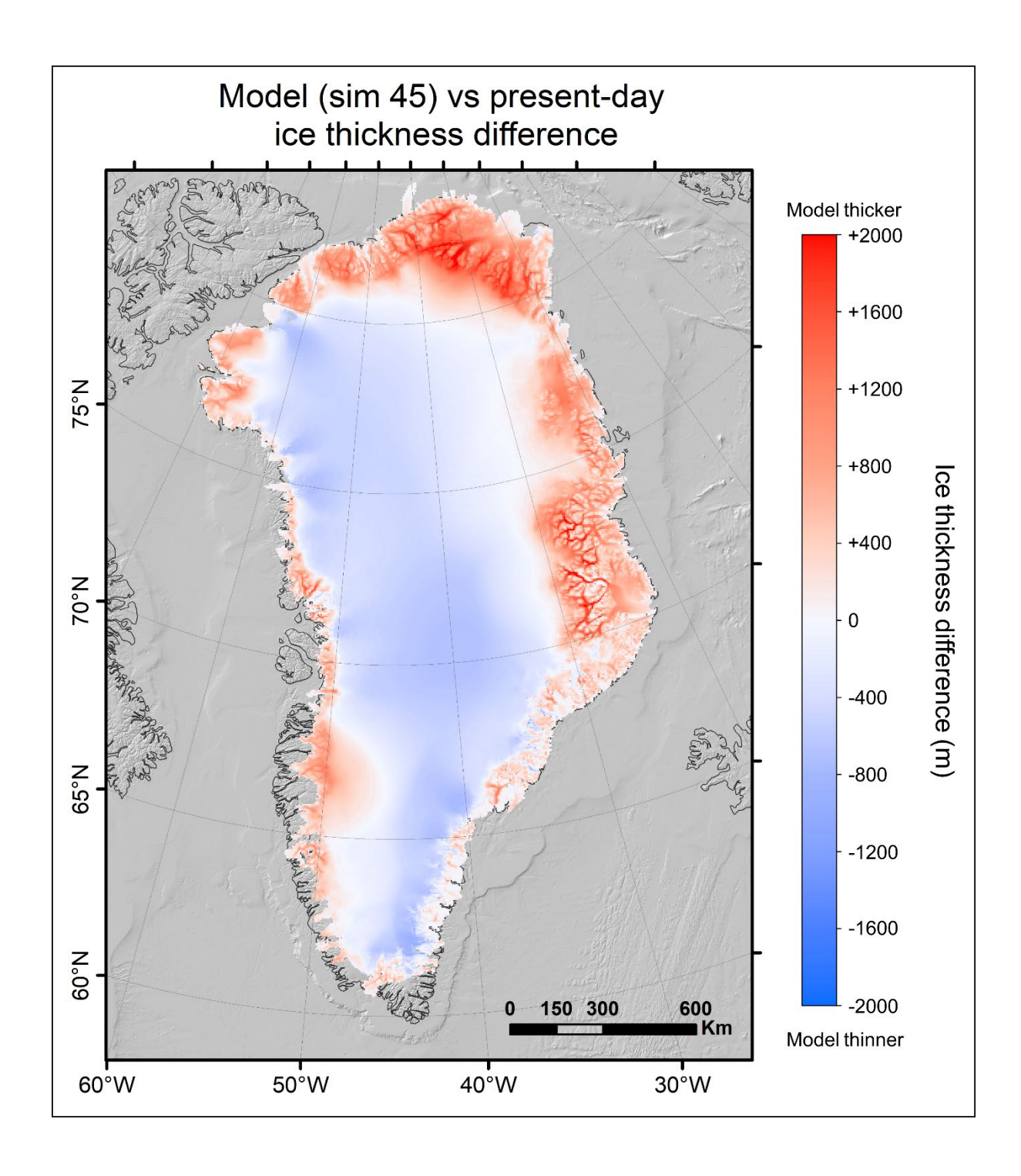


**Figure S15**: GrIS thickness difference between modelled PI states versus the reconstructed present-day GrIS ice thickness (BedMachine v4) for one of the 5 overall best-fit ensemble simulations (which passes all sieves), *i.e.* simulation 45.

## **References:**

Aschwanden, A., Fahnestock, M. A., and Truffer, M.: Complex Greenland outlet glacier flow captured, Nat Commun, 7, 10524, https://doi.org/10.1038/ncomms10524, 2016.

Bennike, O., Björck, S., Böcher, J., Hansen, L., Heinemeier, J., and Wohlfarth, B.: Early Holocene plant and animal remains from North-east Greenland, J Biogeogr, 26, 667–677, https://doi.org/10.1046/j.1365-2699.1999.t01-1-00315.x, 1999.

Håkansson, L., Briner, J., Alexanderson, H., Aldahan, A., and Possnert, G.: 10Be ages from central east Greenland constrain the extent of the Greenland ice sheet during the Last Glacial Maximum, Quat Sci Rev, 26, 2316–2321, https://doi.org/10.1016/j.quascirev.2007.08.001, 2007.

Joughin, I., Smith, B., Howat, I., and Scambos, T.: MEaSUREs Greenland Ice Sheet Velocity Map from InSAR Data, Version 2, 2018.

Leger, T. P. M., Clark, C. D., Huynh, C., Jones, S., Ely, J. C., Bradley, S. L., Diemont, C., and Hughes, A. L. C.: A Greenland-wide empirical reconstruction of paleo ice sheet retreat informed by ice extent markers: PaleoGrIS version 1.0, Climate of the Past, 20, 701–755, https://doi.org/10.5194/cp-20-701-2024, 2024.

Leger, T. P. M., Jouvet, G., Kamleitner, S., Mey, J., Herman, F., Finley, B. D., Ivy-Ochs, S., Vieli, A., Henz, A., and Nussbaumer, S. U.: A data-consistent model of the last glaciation in the Alps achieved with physics-driven AI, Nat Commun, 16, 848, https://doi.org/10.1038/s41467-025-56168-3, 2025.

Marienfeld, P.: Faziesvariationen glazialmariner Sedimente im Scoresby-Sund, Ost-Grönland, Zentralblatt für Geologie und Paläontologie, 1, 1739–1749, 1990.

Morlighem, M., Williams, C. N., Rignot, E., An, L., Arndt, J. E., Bamber, J. L., Catania, G., Chauché, N., Dowdeswell, J. A., Dorschel, B., Fenty, I., Hogan, K., Howat, I., Hubbard, A., Jakobsson, M., Jordan, T. M., Kjeldsen, K. K., Millan, R., Mayer, L., Mouginot, J., Noël, B. P. Y., O'Cofaigh, C., Palmer, S., Rysgaard, S., Seroussi, H., Siegert, M. J., Slabon, P., Straneo, F., van den Broeke, M. R., Weinrebe, W., Wood, M., and Zinglersen, K. B.: BedMachine v3: Complete Bed Topography and Ocean Bathymetry Mapping of Greenland From Multibeam Echo Sounding Combined With Mass Conservation, Geophys Res Lett, 44, 11,051-11,061, https://doi.org/10.1002/2017GL074954, 2017.

Swift, D. A., Persano, C., Stuart, F. M., Gallagher, K., and Whitham, A.: A reassessment of the role of ice sheet glaciation in the long-term evolution of the East Greenland fjord region, Geomorphology, 97, 109–125, https://doi.org/10.1016/j.geomorph.2007.02.048, 2008.